Journal of Geophysical Research: Solid Earth

RESEARCH ARTICLE
10.1029/2018JB015943

Fracture Properties of Nash Point Shale as a Function of Orientation to Bedding

Nathaniel D. Forbes Inskip[1,2], Philip G. Meredith[2], Michael R. Chandler[3], and Agust Gudmundsson[1]

[1]Department of Earth Science, Royal Holloway, University of London, Egham, UK, [2]Department of Earth Sciences, University College London, London, UK, [3]School of Earth and Environmental Sciences, University of Manchester, Manchester, UK

Key Points:
- Measurements of tensile strength and mode-I fracture toughness (K_{Ic}) show that Nash Point shale is mechanically highly anisotropic
- We find that a fracture energy (G_c) approach is more suitable than using K_{Ic} alone, because it allows analysis of mixed mode fracture propagation
- An elliptical function can be used to estimate G_c for fractures propagating at angles between the Short-transverse and Arrester directions

Supporting Information:
- Supporting Information S1

Correspondence to:
N. D. Forbes Inskip, nathaniel.forbesinskip.2014@live.rhul.ac.uk

Citation:
Forbes Inskip, N. D., Meredith, P. G., Chandler, M. R., & Gudmundsson, A. (2018). Fracture properties of Nash Point shale as a function of orientation to bedding. *Journal of Geophysical Research: Solid Earth*, *123*, 8428–8444. https://doi.org/10.1029/2018JB015943

Received 13 APR 2018
Accepted 15 SEP 2018
Accepted article online 20 SEP 2018
Published online 9 OCT 2018

Abstract Understanding how fracture networks develop in shale formations is important when exploiting unconventional hydrocarbon reservoirs and analyzing the integrity of the seals of conventional and carbon capture and storage reservoirs. Despite this importance, experimentally derived fracture data for shale remains sparse. Here we characterize shale from Nash Point in South Wales, United Kingdom, in terms of ultrasonic wave velocities, tensile strength, and fracture toughness (K_{Ic}). We measure these properties in multiple orientations, including angles oblique to the three principal fracture orientations—Short-transverse, Arrester, and Divider. We find that the Nash Point shale is mechanically highly anisotropic, with tensile strength and K_{Ic} values lowest in the Short-transverse orientation and highest in the Arrester and Divider orientations. Fractures that propagate in a direction oblique or normal to bedding commonly deflect toward the weaker Short-transverse orientation. Such deflected fractures can no longer be considered to propagate in pure mode-I. We therefore present a method to correct measured K_{Ic} values to account for deflection by calculating mode-I and mode-II *deflection* stress intensities (K_{Id} and K_{IId}, respectively). Because of the mixed-mode nature of deflected fractures, we adopt a fracture (G_c) energy-based approach that allows analysis of critical fracture propagation conditions for both deflected and undeflected fractures in all orientations. We find that G_c increases as the angle from the Short-transverse plane increases. We conclude that a modified elliptical function, previously applied to tensile strength and K_{Ic}, can be used to estimate values of G_c at angles between the Short-transverse and Arrester orientations.

1. Introduction

Shales, as a class, are the most abundant of sedimentary rock types, making up more than 50% of sedimentary material worldwide (Chandler et al., 2016). They are important not only as source rocks and seals in conventional hydrocarbon systems, but also as seals for potential carbon capture and storage reservoirs (Levine et al., 2016), as well as being both source and reservoir rocks in unconventional gas plays (Boyer et al., 2011). Specifically, over the past decade or so, there has been an increased emphasis on producing hydrocarbons from unconventional resources such as gas shales. This involves hydraulically fracturing these formations in order to increase the overall reservoir permeability.

Despite the importance and increased interest in shales, there remains a paucity of data describing their mechanical and physical properties, in particular, when compared with the amount of available data on other sedimentary rocks, such as sandstones and limestones. The paucity of data on shales is especially noticeable regarding their fracture mechanical properties (tensile strength, fracture toughness, and fracture energy). Part of the reason for this lack of data is that their mineralogy, microstructure, and inherent anisotropy mean that shales are difficult materials to work with (Chandler, 2014; Islam & Skalle, 2013).

Apart from environmental parameters such as the in situ stress field, pore fluid pressure, and the fracturing fluid pressure (Warpinski & Smith, 1990), the key material parameters involved in hydraulic fracturing are tensile strength, which controls fracture initiation, and tensile (mode-I) fracture toughness, which controls fracture propagation. Most sedimentary rocks exhibit some form of structural anisotropy, which is either the result of their depositional environment and the alignment of mineral grains, or is caused by the alignment of pores or microfractures. Such structural anisotropy commonly results in physical and mechanical anisotropy (Chandler et al., 2016; Chong et al., 1987; Kabir et al., 2017; Lee et al., 2015; Schmidt,

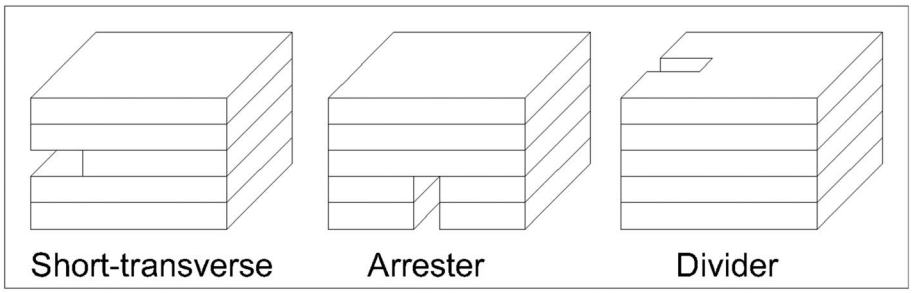

Figure 1. The three principal fracture orientations with regard to bedding planes: Short-transverse, Arrester, and Divider. Modified after Chong et al. (1987).

1977; Young et al., 1982). Therefore, many sedimentary rocks, including shales, exhibit transverse isotropy parallel to their bedding planes. We would thus expect their tensile strength and fracture toughness values also to be anisotropic. When considering the growth of essentially planar fractures in a material with a planar fabric, we can define three principal fracture orientations: Short-transverse, Arrester, and Divider (as illustrated in Figure 1; Chong et al., 1987). In the Short-transverse orientation both the fracture plane and fracture propagation direction are parallel to bedding. Conversely, in the Arrester orientation both the fracture plane and the fracture propagation direction are normal to bedding. Finally, in the Divider orientation the fracture plane is normal to bedding while the fracture propagation direction is parallel to bedding.

While there have been numerous reports of tensile strength anisotropy in layered rocks (e.g., Islam & Skalle, 2013; Li et al., 2017; Rybacki et al., 2015; Tavallali & Vervoort, 2013), there have been relatively few reported measurements of fracture toughness anisotropy in such rocks. This is particularly true for shales, for which only a handful of studies to date report data on the fracture toughness in more than one orientation (Chandler et al., 2016; Kabir et al., 2017; Lee et al., 2015; Schmidt, 1977). Schmidt (1977) measured the fracture toughness of Anvil Points shale in all three principal orientations using a three-point-bending methodology on samples which had previously been fatigue cracked. Schmidt (1977) also investigated the effect of kerogen content on the fracture toughness by testing specimens containing 80 ml/kg and 160 ml/kg of kerogen. It was found that specimens with a higher kerogen content had a significantly lower fracture toughness, in all three principal orientations. For specimens containing 80 ml/kg of kerogen the fracture toughness of samples tested in the Divider orientation was found to be the highest (1.08 MPa $m^{1/2}$) and samples tested in the Short-transverse orientation was found to be the lowest (0.75 MPa $m^{1/2}$). Samples tested in the Arrester orientation had a fracture toughness of 0.98 MPa.$m^{1/2}$, slightly lower than that for specimens tested in the Divider orientation. This trend was also observed when testing specimens containing 160 ml/kg of kerogen where the fracture toughness of samples tested in the Divider, Short-transverse, and Arrester orientations were 0.67 MPa $m^{1/2}$, 0.37 MPa $m^{1/2}$, and 0.60 MPa $m^{1/2}$, respectively.

Lee et al. (2015) measured the fracture toughness of samples of Marcellus shale in the Divider and Arrester orientations, and also in a direction 30° from the Arrester orientation, using the semicircular bend (SCB) methodology (Kuruppu et al., 2014). They found that the fracture toughness in the Arrester orientation (0.73 MPa $m^{1/2}$) was significantly higher than that in the Divider orientation (0.47 MPa $m^{1/2}$), but that the lowest value was obtained for fractures propagating at 30° to the Arrester orientation (0.18 MPa $m^{1/2}$). Chandler et al. (2016) reported fracture toughness data for Mancos shale in all three principal orientations, measured using the short rod (SR) methodology (International Society for Rock Mechanics, 1988). In contrast to Lee et al. (2015) they found the fracture toughness values in both the Arrester and Divider orientations to be the same at 0.44 MPa $m^{1/2}$, while the fracture toughness in the Short-transverse orientation was both significantly lower and also exhibited a bimodal distribution; 0.12 MPa $m^{1/2}$ and 0.31 MPa $m^{1/2}$. Optical and scanning electron microscopy of Mancos shale revealed layers of two distinctly different materials; fine-grained clay layers interwoven with coarser-grained silt layers. Chandler et al. (2016) postulated that in some of the Short-transverse samples tested the fracture propagated along a weaker clay layer, while in others, it propagated along a stronger silt layer and that this was the likely explanation for the bimodal fracture toughness distribution observed for this orientation.

Figure 2. (left) Map of Wales showing the location of Nash Point. (right) Cliff section at Nash Point demonstrating the interbedded shaly mudstones and limestone sequence. Cliff height in the background is approximately 30 m.

Kabir et al. (2017) report values of the fracture toughness of Niobrara shale from northeastern Colorado and Toarcian shale from the Paris basin, calculated indirectly using data from scratch and indentation tests. The calculated values for Niobrara shale range from 4.40 MPa $m^{1/2}$ in the Short-transverse orientation to 5.26 MPa $m^{1/2}$ in the Divider orientation. For Toarcian shale, they were only able to calculate fracture toughness in the Short-transverse orientation, and give a value of 4.06 MPa $m^{1/2}$. These calculated values are all close to an order of magnitude higher than those measured directly and reported by other workers.

To our knowledge, there has been no study to date that has systematically considered fracture nucleation and propagation in orientations other than the three principal ones. Here we report the results of a study in which we have measured both tensile strength and fracture toughness on samples of Nash Point shale in the three principal orientations and at intervals of 15° between the Short-transverse and Arrester orientations. We used the Brazil disk technique to measure tensile strength and the SCB methodology to measure fracture toughness. We also provide an analysis for calculating values of the fracture energy from measured fracture toughness values when fractures are observed to become deflected from their intended propagation direction.

2. Sample Material and Characterization

2.1. Mineralogy and Microstructure

In this study, we measure and analyze physical and mechanical properties of Nash Point shale, which is the shaly member of the Porthkerry Formation, outcropping at Nash Point on the Glamorganshire coast of Wales (Figure 2, left). The Porthkerry Formation is Hettangian-Sinermurian in age and is characterized by a sequence of interbedded shaly mudstones and limestones. Based on vitrinite reflectance data (Cornford, 1986), it is considered to have reached a maximum burial depth of 3.2 km during the Aptian.

The cliff section at Nash Point is approximately 30 m high and is laterally continuous for several kilometers (Figure 2, right). Mineral veins are common throughout, occurring over a range of scales from thicknesses of less than a millimeter and lengths (strike dimensions) of several centimeters to thicknesses in excess of several centimeters and lengths up to many meters. The latter primarily occur within the damage zones of faults and generally strike parallel or subparallel to the faults with which they are associated.

Thin section analysis demonstrates that Nash Point shale is moderately sorted, with grains that are predominately subangular and exhibit strong alignment within a clay matrix (Figure 3). The great majority of the grains are shell fragments, with a significant proportion of quartz grains also present. The shell fragments range in size from about 0.1 to 4 mm, with many appearing to originate from bivalves and some containing chert fragments. X-ray diffraction (XRD) analysis shows that Nash Point shale is composed predominately of calcite (50–70%), with lesser amounts of clay (20–30%) and quartz (10–20%).

The Nash Point shale used in this study had a porosity of ~6.5%, measured using helium pycnometry (Chalmers & Bustin, 2017; Chandler et al., 2016; Heap et al., 2009) and a bulk density of 2,430 kg/m^3.

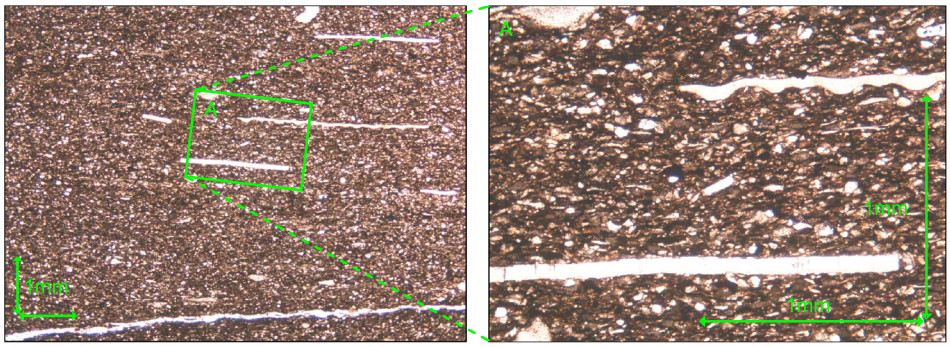

Figure 3. (left) Thin section of Nash Point shale with 1-mm bars for scale. (right) Inset area of thin section image on the left.

While Nash Point shale is not a pure *shale* petrologically, it does share many of the features of other well-known gas shales and, in particular, those of the Eagle Ford shale formation (Texas, USA), which is a major unconventional oil and gas play. The mineralogy of Eagle Ford shale has been studied by numerous authors (including Chalmers & Bustin, 2017; Elston, 2014; Knorr, 2016; Milliken et al., 2016; Mokhtari, 2015; Mullen et al., 2010), and the same general mineralogy is observed, with Eagle Ford shale also being dominated by calcite with lesser amounts of clay, and quartz. For means of comparison, Chalmers and Bustin (2017) found that Eagle Ford shale contained 32–87% calcite (average of 57%), 2–38% clay (average of 17%), and 6–20% quartz (average of 14%). Porosities were found to be between 3.5 and 10.3%, with an average value of 7.5%. These data were measured on core gathered from a depth of 4.1–4.2 km.

It is well known that shales often exhibit significantly greater mechanical anisotropy in outcrop samples than in subsurface (e.g., borehole) samples, particularly due to weathering effects and mineral alteration. However, we note that Knorr (2016) conducted XRD analysis on outcrop samples of Eagle Ford shale and found essentially the same mineralogical composition as that for the subsurface (borehole) samples reported above, suggesting that weathering had not altered the mineralogy in any significant way. No subsurface XRD data are available for Nash Point shale to make a similar comparison. However, the outcrop from which our Nash Point shale samples were taken occurs on a wave cut platform which is continuously eroded by the sea (both from wave action and the exceptionally high tidal range of the Bristol Channel). New rock surfaces are therefore unlikely to be exposed to weathering for any great length of time, so we consider any weathering effect on our samples to be minimal. Hence, based on this, and its similarity to Eagle Ford shale, we consider the mineralogy of the Nash Point shale outcrop material used in this study to be a reasonable approximation to the same material in the subsurface.

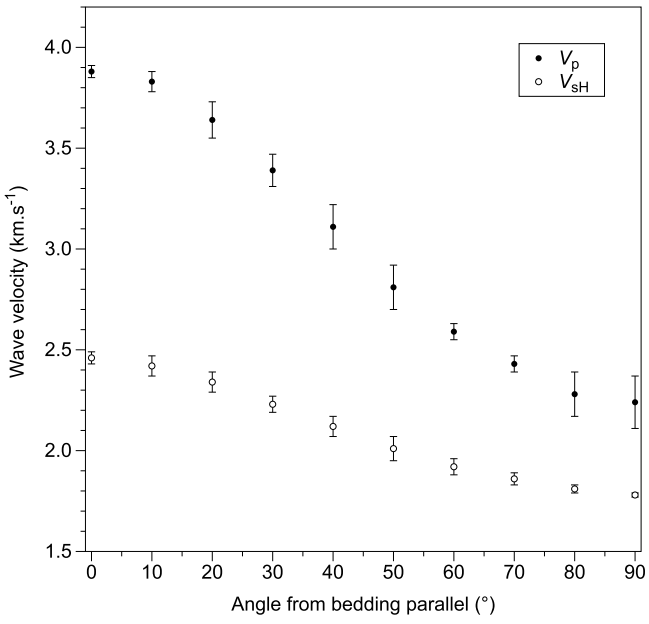

Figure 4. Ultrasonic *P* and *S* wave velocities of Nash point shale as a function of angle from bedding parallel.

2.2. Elastic Anisotropy

We characterized the anisotropy of Nash point shale by measuring the *P* wave and *S* wave velocities across the diameter of 38-mm cylindrical samples under dry, ambient pressure and ambient temperature conditions. Velocities were measured in 10° increments around the full 360° perimeter of two independent samples using the pulse transmission technique (Birch, 1960). Measurements were made using the same testing jig and ultrasonic transducers (with a resonant frequency of 1 MHz) as described by Vinciguerra et al. (2005). This results in a total of eight measurements for each orientation.

The results from all measurements are presented in Figure 4 (mean ± standard deviation), where the *P* wave velocity parallel to bedding (V_{p0}) is 3.88 ± 0.03 km/s and that normal to bedding (V_{p90}) is 2.24 ± 0.13 km/s. These values give a *P* wave velocity anisotropy of 54% calculated from:

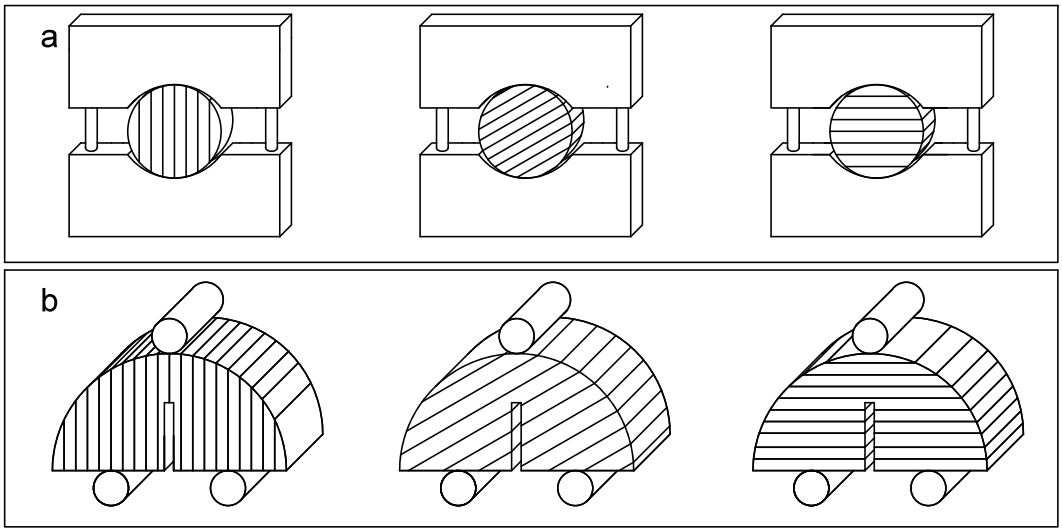

Figure 5. (a) Schematic of Brazil disk test setup where samples are tested in the Short-transverse (left), 60° to bedding (center), and Arrester (right) orientations. (b) Schematic of SCB test set up where samples are again tested in the Short-transverse (left), 60° to bedding (center), and Arrester (right) orientations. In each case the solid black lines on the samples depict bedding plane orientation.

$$\frac{V_{max} - V_{min}}{V_{mean}} \quad (1)$$

By comparison, the *S* wave velocity parallel to bedding (V_{sH0}) is 2.46 ± 0.03 km/s and that normal to bedding (V_{sH90}) is 1.78 ± 0.01 km/s. These values give an *S* wave velocity anisotropy of 32%. These values of anisotropy are high, even for shale. For example, Chandler (2014) found the Mancos shale to have a *P* wave velocity anisotropy of 22% and an *S* wave velocity anisotropy of 11%.

All our measurements were of phase velocities, but seismic dispersion should be negligible in a dry, low permeability rock such as Nash Point shale. Furthermore, it has been shown by Johnston and Christensen (1995) and Dewhurst and Siggins (2006) that the maximum difference between phase and group velocity under these conditions is less than 5%.

3. Sample Preparation and Experimental Methodology

3.1. Tensile Strength Measurements

The Brazil disk test methodology (International Society for Rock Mechanics, 1978) was used to measure the indirect tensile strength of samples of Nash Point shale measuring 38 mm in diameter by 19 mm in thickness. All samples were cored from a single block of material, and their surfaces ground flat and parallel to within 0.02 mm using a surface grinder. The bedding plane orientation was marked on all samples. Tensile strength measurements were then made in all three principal orientations and at intervals of 15° between the Short-transverse and Arrester orientations by simply rotating the sample disks between the loading platens (Figure 5a). It should be noted that in this study we quote values at orientations from bedding parallel, while in some studies values may be quoted at orientations from the axis of rotational symmetry, which in this case would be the bedding normal orientation. All samples were deformed by diametral loading at a constant displacement rate of 0.1 mm/min using a Brazil test jig mounted within a servo-controlled loading frame. This resulted in test durations from around 1 to 2 min, commensurate with International Society for Rock Mechanics (ISRM) recommendations. A minimum of four samples was tested in each orientation.

3.2. Fracture Toughness Measurements

The ISRM has published four suggested methods for measuring the mode I fracture toughness of rock; each of which has advantages and disadvantages. We elected to use the ISRM SCB methodology (Kuruppu et al., 2014) for our experiments, because it is efficient in terms of both material usage and in allowing for angles

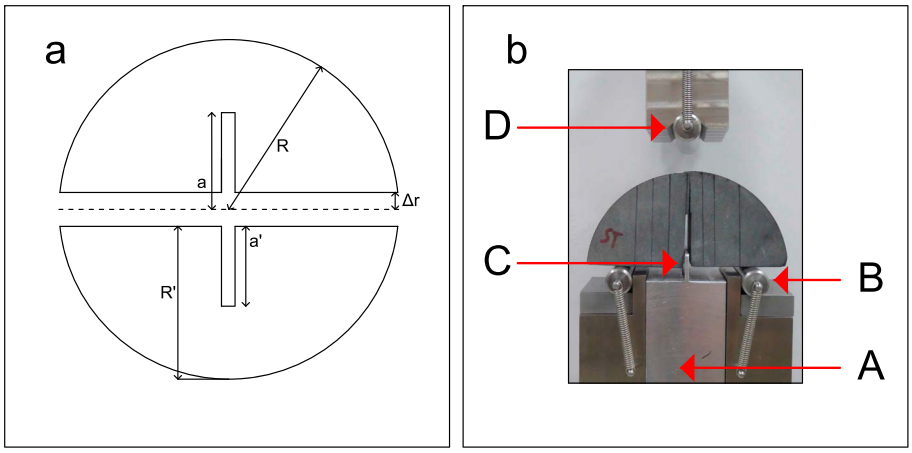

Figure 6. (a) Schematic of dimensions for a standard SCB sample after a circular disk has been cut in two. Here R is the notional radius, R' is the reduced radius, a is the notional notch length, a' is the modified notch length and $\Delta r = R - R'$. Modified after Kuruppu et al. (2014). (b) Photo of finished sample in the loading jig; where A is the alignment block, B is one of the two bottom rollers, C is the central blade, and D is the moving top roller.

between the Short-transverse and Arrester orientations to be measured relatively easily by simply cutting samples in different orientations (Figure 5b).

SCB samples were prepared in accordance with the geometry and dimensions suggested in Kuruppu et al. (2014). Samples were manufactured from 76-mm-diameter cores taken either normal or parallel to bedding. Each core was then cut into slices, which were ground flat and parallel to within 0.02 mm to produce disks of nominal thickness 30 mm.

Each 30-mm disk was subsequently cut in half using a diamond saw to create two quasi-semicircular samples, and the central saw-cut surfaces were ground flat using a surface grinder. This results in two samples that are less than fully semicircular due to the loss of material from the cutting and grinding processes. To complete each sample, a straight-cut notch was sawn into the center of the newly ground surface and perpendicular to it. The notional depth of the notch, a, must satisfy the following relation:

$$0.4 \leq \frac{a}{R} \leq 0.6 \tag{2}$$

where R is the notional sample radius. For this study, the notional radius was 38 mm and the notional notch depth was 22 mm so that $a/R = 0.58$. However, the loss of material from the cutting and grinding needs to be taken into account and the notch depth modified accordingly. This is achieved by measuring the reduced radius of the sample in the plane of the notch, R' and calculating the modified notch depth, a' where $a' = a - \Delta r$ and, $\Delta r = R - R'$. This results in a modified (actual) notch depth of 20 mm. Details of the geometry and dimensions of the SCB samples used in this study are given in Figure 6a. Use of these sample dimensions results in a fracture-front length of 30 mm and a total fracture area of 480 mm^2. Taking the geometric mean of the grain size range of Nash Point shale (0.6 mm), this means that the propagating fracture front spans an average of 50 grain diameters and that the fracture samples an average of some 1,300 grains during its propagation. We therefore suggest that the results of our experiments are fully representative of the fracture properties of the test material.

Figure 6b shows a Short-transverse-orientated SCB sample located within the testing jig. Sample positioning and alignment are controlled by a specially designed alignment block (A in Figure 6b). The width of the alignment block controls the span between the two bottom rollers (B in Figure 6b) which is set to a fixed value of 50 mm. A central blade on the alignment block (C in Figure 6b) that fits into the sample notch controls the centralization of the sample between the bottom rollers and also ensures that the sample is aligned at right angles to the rollers. The alignment blade is sufficiently short so as not to interfere with the sample during testing. All samples were loaded in three-point-bending via the moving top roller (D in Figure 6b) at a constant displacement rate of 0.1 mm/min, which resulted in test durations of between 60 and 140 s.

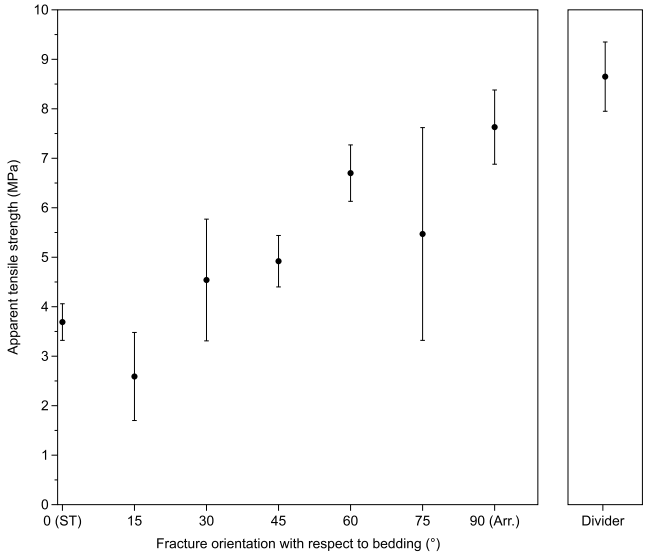

Figure 7. Mean apparent tensile strength (MPa) of Nash Point shale in the three principal orientations (where ST and Arr. refer to the Short-transverse and Arrester orientations, respectively), and at 15° intervals between the Short-transverse and Arrester orientations. Error bars show ±1 standard deviation.

The fracture toughness, K_{Ic}, is then calculated from (Kuruppu et al., 2014)

$$K_{Ic} = Y' \frac{P_{\max}\sqrt{a'\pi}}{2R'B'} \tag{3}$$

where P_{max} is the peak load, a' is the modified notch length, R' is the reduced radius, B' is the sample thickness, and Y' is a nondimensional stress intensity factor that accounts for the specific sample geometry and is as defined below:

$$Y' = -1.297 + 9.516\left(\frac{s}{2R'}\right) - \left[0.47 + 16.457\left(\frac{s}{2R'}\right)\right]\beta + \left[1.071 + 34.401\left(\frac{s}{2R'}\right)\beta^2\right] \tag{4}$$

where s is the span between the two bottom rollers and

$$\beta = \frac{a'}{R'} \tag{5}$$

Using the methodology described above, the fracture toughness of Nash Point shale was measured in the three principal orientations and at angles between the Short-transverse and Arrester orientations in 15° increments. A minimum of four samples was tested in each of the orientations.

4. Results

4.1. Tensile Strength

The tensile strengths of samples of Nash Point shale measured in the three principal orientations and at angles between the Short-transverse and Arrester orientations in 15° increments are given in Figure 7 (mean ± standard deviation)**.** The ISRM suggested method for measuring indirect tensile strength by the Brazil test inherently assumes that the maximum tensile stress occurs at the center of the sample and the tensile fracture therefore nucleates at this point. However, as we discuss later, the fracture in a significant number of our shale samples did not nucleate at or propagate through the center of the sample. Furthermore, a number of workers (e.g., Chen et al., 1998; Claesson & Bohloli, 2002; Na et al., 2017) have proposed that the standard ISRM formulation is not appropriate for anisotropic materials and have suggested a number of alternatives. Since we have used the standard ISRM methodology in this study, we report our results as *apparent tensile strength* in Figure 7. In general, we observe a progressive increase in apparent tensile strength as the fracture angle changes from parallel to the Short-transverse orientation (3.69 MPa) to parallel to the Arrester orientation (7.63 MPa). There is some scatter in the data, with this being highest at angles oblique to the bedding orientation; specifically, at 15°, 30°, and 75°. The standard deviation for these angles as a percentage of the mean value is 34%, 27%, and 39%, respectively, compared with 11%, 10%, 8%, and 10% for angles of 0°, 45°, 60°, and 90° to bedding, respectively. It is perhaps not surprising that the scatter is highest at angles oblique to bedding, because these are the angles where we most commonly observe fractures that do not pass through the sample center, and deflections from the intended fracture orientation. As noted above, this issue is discussed in detail later. The propagation paths of fractures appear to be stable and repeatable at 0°, 45°, and 90°, but less so at these intermediate angles. The highest apparent tensile strength measured was in the Divider orientation (8.65 MPa), but it is somewhat similar to the Arrester orientation (7.63 MPa) and much higher than that measured in the Short-transverse orientation (3.69 MPa).

4.2. Fracture Toughness

Examples of load/displacement curves from tests on samples oriented in the Short-transverse, 45° to bedding and Arrester directions are given in Figure 8. All samples were loaded at the same displacement rate of 0.1 mm/min. For all tests, we observe an initial nonlinear phase due to bedding-in of the components of the loading train. This is followed by the main linear elastic loading phase, which continues until just prior

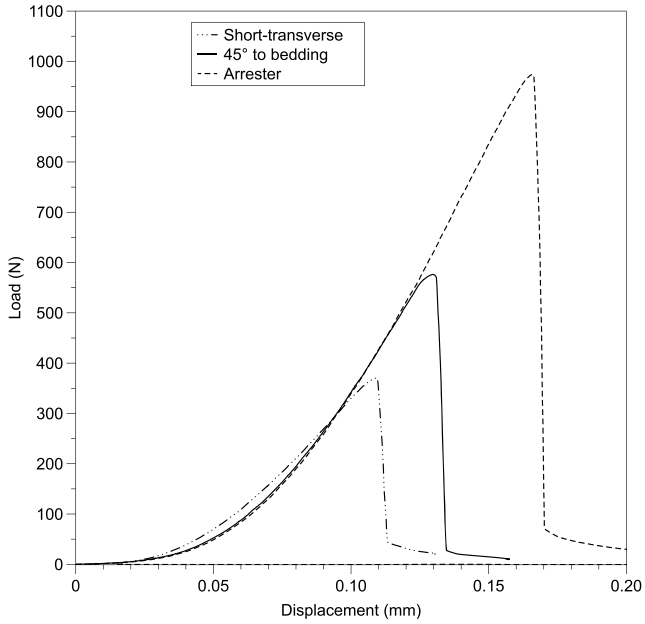

Figure 8. Examples of load-displacement curves for tests conducted on SCB samples oriented at 0° (Short-transverse), 45°, and 90° (Arrester) to bedding.

to failure, where we observe a very short roll-over phase. A key point is that the slopes of the load/displacement curves are very similar during the linear phase even though the samples fail at very different loads. The Arrester sample fails at a load that is close to 3 times higher than that for the Short-transverse sample, with the sample oriented at 45° to bedding failing at an intermediate value. The fracture toughness (K_{Ic}) of Nash Point shale samples measured in all three principal orientations and at angles between the Short-transverse and Arrester orientations in 15° increments are presented in Figure 9 (mean ± standard deviation). Similar to the tensile strength results, we observe a progressive increase in fracture toughness from parallel to the Short-transverse orientation (0.24 MPa $m^{1/2}$) to parallel to the Arrester orientation (0.74 MPa $m^{1/2}$). However, the fracture toughness values are better constrained and exhibit considerably less scatter. Again, the value of the fracture toughness in the Divider orientation (0.71 MPa $m^{1/2}$), is similar to that in the Arrester orientation (0.74 MPa $m^{1/2}$), with both being approximately 3 times higher than the value in the Short-transverse orientation (0.24 MPa $m^{1/2}$).

Of the 38 fracture toughness samples tested, five failed prematurely at anomalously low loads due to fractures propagating along thin calcite veins within the samples, which were generally orientated at high angles (60–90°) to bedding. These anomalous results have therefore been excluded from any further analysis.

For purposes of comparison, the fracture toughness of Nash Point shale was also measured in both the Short-transverse and Divider orientations using the same modified SR methodology described in Chandler et al. (2016) and using the same testing jigs and fixtures. The fracture toughness values from both methodologies are entirely consistent, and a synopsis of all the tensile strength and fracture toughness data measured in this study is presented in Table 1.

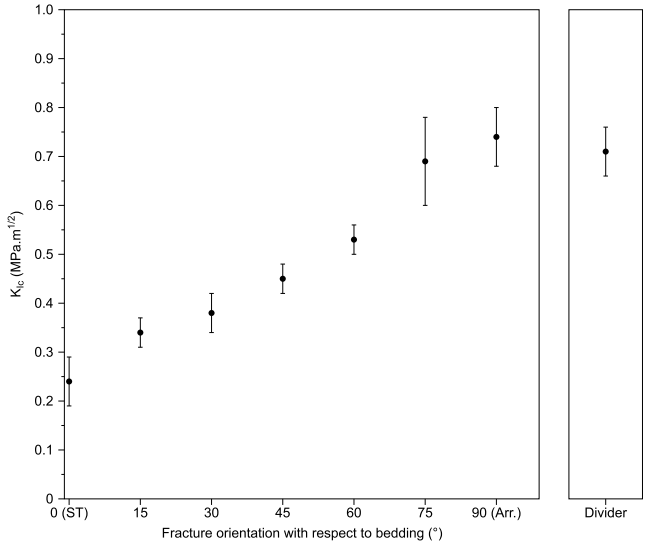

Figure 9. Mean fracture toughness, K_{Ic} (MPa $m^{1/2}$), of Nash Point shale in the three principal orientations (where ST and Arr. refer to the Short-transverse and Arrester orientations, respectively), and at 15° intervals between the Short-transverse and Arrester orientations. Error bars show ±1 standard deviation.

5. Discussion

5.1. Influence of Orientation on Fracture Properties

It is clear from Figure 7 that the apparent tensile strength of Nash Point increases progressively from samples tested in the Short-transverse orientation to those tested in the Arrester orientation. This is not surprising because the propagating fracture must traverse more interfaces (layers) as the angle to bedding is increased and all of the available interfaces when propagating in the Arrester orientation. By contrast, the fracture will ideally propagate along only a single layer in the Short-transverse orientation. In reality, however, the bedding layers are rarely perfectly parallel, and Short-transverse fractures may therefore need to traverse a small number of interfaces as they propagate. At some of the intermediate angles there is a significant degree of scatter in the data, particularly at 30° and 75° to bedding. Postmortem inspection of the fractures in these samples reveals that (i) they commonly do not pass through the center of the sample, and (ii) they commonly deflect away from the intended (load-parallel) direction toward the weaker Short-transverse (bedding-parallel) direction for at least part of the propagation pathway. An example of both occurrences is given in Figure 10. We suggest that this competition between propagation in the direction of the applied stress and propagation along the weak bedding plane may well be responsible for the higher degree of scatter observed at these intermediate angles.

Table 1
Summary of the Mean Apparent Tensile Strength and Fracture Toughness of Nash Point Shale in the Three Principal Fracture Orientations and at 15° Intervals Between the Short-Transverse and Arrester

Orientation with respect to bedding plane	Apparent tensile strength (MPa)	K_{Ic}, [SCB] (MPa $m^{1/2}$)	K_{Ic}, [SR] (MPa $m^{1/2}$)
0° (Short-transverse)	3.69 ± 0.37	0.24 ± 0.05	0.30 ± 0.09
15°	2.59 ± 0.89	0.34 ± 0.03	—
30°	4.54 ± 1.23	0.38 ± 0.05	—
45°	4.92 ± 0.52	0.45 ± 0.03	—
60°	6.70 ± 0.57	0.53 ± 0.03	—
75°	5.47 ± 2.15	0.69 ± 0.09	—
90° (Arrester)	7.63 ± 0.75	0.74 ± 0.06	—
Divider	8.65 ± 0.70	0.71 ± 0.05	0.73 ± 0.06

Note. It was only possible to measure the fracture toughness in the Short-transverse and Divider orientations using the short-rod (SR) methodology. However, the measured values in these orientations are in good agreement with the corresponding values using the semicircular bend (SCB) methodology.

The fracture toughness data presented in Figure 9 exhibit similar characteristics to those of the tensile strength data (Figure 8), but with significantly less scatter. Again, there is a progressive increase in values from samples tested in the Short-transverse orientation to those tested in the Arrester orientation; with the Arrester orientation values being some 3 times higher than the Short-transverse value. However, values for the Arrester and Divider orientations are essentially the same. This is entirely as expected, because the fracture necessarily traverses all of the available interfaces in both of these orientations. In the Arrester orientation all of the interfaces are sampled sequentially, while in the Divider orientation they are all sampled simultaneously.

5.2. Comparison of the Fracture Properties of Nash Point Shale With Those of Other Shales

Fracture toughness values for a range of shales are presented in Table 2; taken from the literature, where values were directly measured in more than one principal orientation. The K_{Ic} values measured in this study for Nash Point shale all lie within the range of values for other shales listed in Table 2. Furthermore, the data from all of the studies where K_{Ic} was measured in all three principal orientations (Schmidt, 1977; Chandler et al., 2016; this study) demonstrate a very similar relationship; with K_{Ic} values for the Arrester and Divider orientations being generally very similar, but much higher than values for the Short-transverse orientation.

From the Griffith criterion (Paterson & Wong, 2005), we can write the following relationship between tensile strength and mode-I fracture toughness:

$$\sigma_t = C\frac{K_{Ic}}{\sqrt{a}} \tag{6}$$

where σ_t is tensile strength, C is a dimensionless geometric factor, and a is a characteristic flaw size. Previous compilations have shown that a broadly linear relationship exists between K_{Ic} and the tensile strength of numerous rock types (e.g., Bhagat, 1985; Chandler et al., 2016; Gunsallus & Kulhawy, 1984; Zhang, 2002). We illustrate this relationship for shales in Figure 11, where both K_{Ic} and tensile strength data were available for the same rock in the same study (Chandler et al., 2016; Chong et al., 1987; Schmidt, 1977). Note that data from Chong et al. (1987) are included in Figure 11, but were not included in Table 2 as values were only measured in a single orientation. The data of Figure 11 include values from tests in the three principal fracture orientations, together with values from this study measured at angles between the Short-transverse and Arrester orientations. A linear least squares fit to the data of Figure 11 is found to have a gradient of 13.7 $m^{-1/2}$ with an associated R^2 value of 0.71. As previously discussed by Chandler et al. (2016), where the K_{Ic} versus σ_t relationship is essentially linear, this implies that the characteristic flaw size controlling fracture nucleation is essentially the same between the different shale formations and the different fracture orientations.

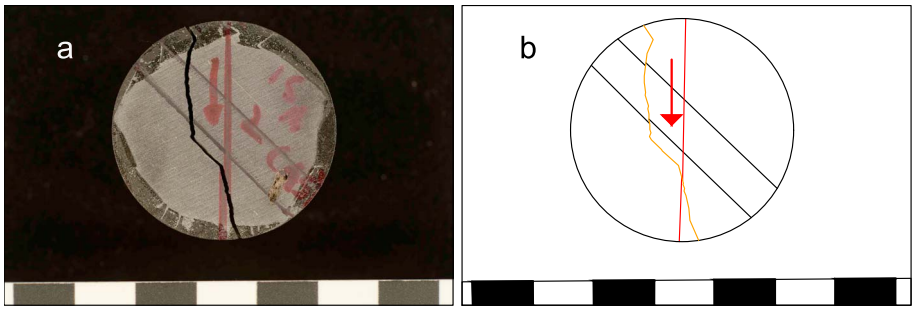

Figure 10. (a) Photo and (b) corresponding schematic sketch of a tested Brazil disk sample demonstrating how the induced fracture (orange) steps between the bedding plane (solid black lines across the sample) and the loading direction (red arrow).

Table 2
Summary of K_{Ic} Values From This Study and Others in Which K_{Ic} was Directly Measured in More Than One of the Principal Fracture Orientations

Material	K_{Ic}, Short-transverse (MPa m$^{1/2}$)	K_{Ic}, Arrester (MPa m$^{1/2}$)	K_{Ic}, Divider (MPa m$^{1/2}$)	Methodology	Reference
Nash Point shale	0.24	0.74	0.71	SCB	This study
Nash Point shale	0.3	—	0.73	Short-rod	This study
Mancos shale[a]	0.12 (ST_{low}); 0.31 (ST_{high})	0.44	0.44	Short-rod	Chandler et al. (2016)
Marcellus shale	-	0.73	0.47	SCB	Lee et al. (2015)
Anvil Points shale (80 ml/kg kerogen content)	0.75	0.98	1.08	Three-point bending	Schmidt, (1977)
Anvil Points shale (160 ml/kg kerogen content)	0.37	0.60	0.67	Three-point bending	Schmidt (1977)

Note. SCB = semicircular bend.
[a]Chandler et al. (2016) found that the K_{Ic} measured in the Short-transverse orientation had a bimodal distribution, and so both values are given in this table.

5.3. Fracture Orientation and Tortuosity

Postmortem examination of samples from both fracture toughness and tensile strength tests shows that fractures propagating in the Short-transverse and Divider orientations are relatively straight in comparison with those propagating in other orientations (Figures 12 and 13). Deflection of the induced fractures away from the loading direction and toward the Short-transverse orientation is common both in samples tested at intermediate angles (Figure 12) and in those tested in the Arrester orientation (Figure 13). In comparison with undeflected fractures, we observe that deflected fractures are more tortuous, and we suggest that this tortuosity is again due to competition between the orientation of the applied load and the orientation of the weak Short-transverse orientation throughout the propagation of the fracture.

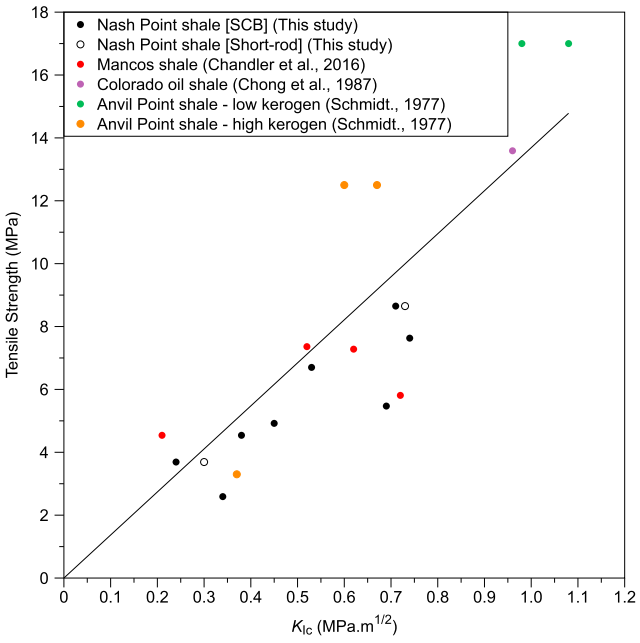

Figure 11. The relationship between tensile strength and fracture toughness of different shale formations (Chandler et al., 2016; Chong et al., 1987; Schmidt, 1977). The solid line is a linear least squares fit to the data, with a forced intercept of zero, a gradient of 13.7 m$^{-1/2}$, and an R^2 value of 0.71.

This phenomenon has also been reported by Tavallali and Vervoort (2013), from a study in which they analyzed the fracture patterns produced from Brazil disk tensile tests on a transversely isotropic layered sandstone from Modave (southern Belgium). Tavallali and Vervoort (2013) conducted tests over a range of angles between bedding parallel and bedding normal and report that different modes of fracture occurred at the different angles. They therefore report their values as *Failure strengths* rather than *Tensile strengths*. Furthermore, we have noted earlier that a significant number of the fractures in our Brazil disk tensile strength tests did not pass through the center of the sample. This was also reported by Tavallali & Vervoort, 2013) and Na et al. (2017). Consequently, we conclude that we cannot be confident that the failure loads in these tests correspond to the true tensile strength, and we have therefore reported the results as *apparent tensile strength*. At the time of writing we know of no method that can be used to correct such tensile strength values to account for fracture deflections. However, we have developed a method that can be used to correct fracture toughness values when the fracture is deflected from its intended propagation direction; and we present this analysis below. Overall, we therefore consider fracture toughness to be a more fundamental and rigorous measure of the resistance to tensile fracture propagation, especially in anisotropic materials such as shales.

5.4. Determination of the Point at Which Fracture Toughness Is Evaluated

In Figure 14, we plot the dimensionless stress intensity factor for the SCB specimen (from equation (4)), Y', as a function of the dimensionless

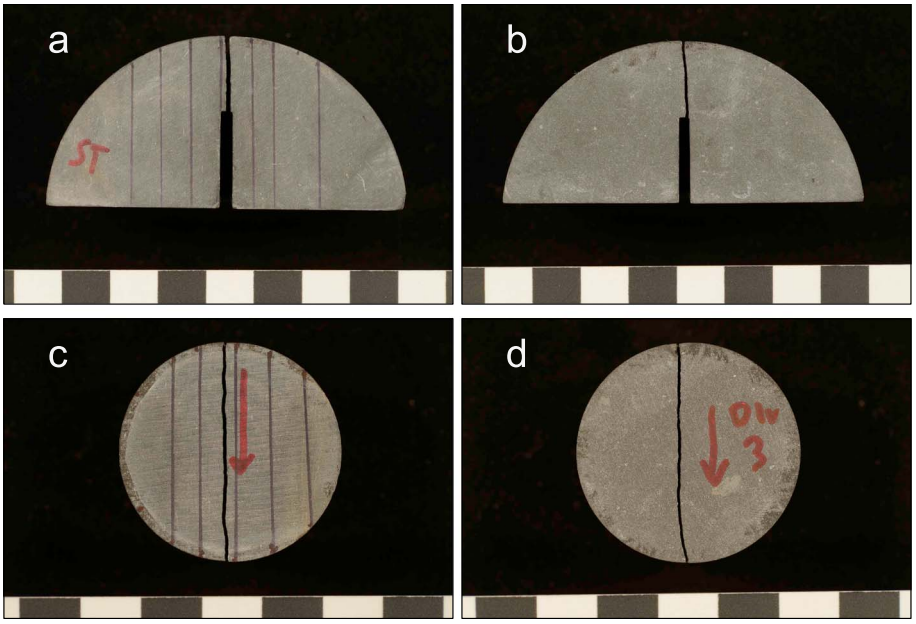

Figure 12. SCB and Brazil disk samples tested in the Short-transverse (12a, 12c) and Divider (12b, 12d) orientations. Solid black lines show the orientation of the bedding plane and a scale bar lies below each sample where each division is 1 cm. Fractures in these orientations are straight and propagate both parallel to the loading orientation and bedding plane.

fracture length, β, for a sample with the dimensions used in this study. The red circle shows the values of Y' and β for our sample dimensions with a notional notch depth of 22 mm. In the region where the dimensionless stress intensity is decreasing as a function of increasing fracture length (left of the vertical dashed line), the fracture propagation is inherently stable. By contrast, in the region where the dimensionless stress intensity is increasing as a function of increasing fracture length (right of the vertical

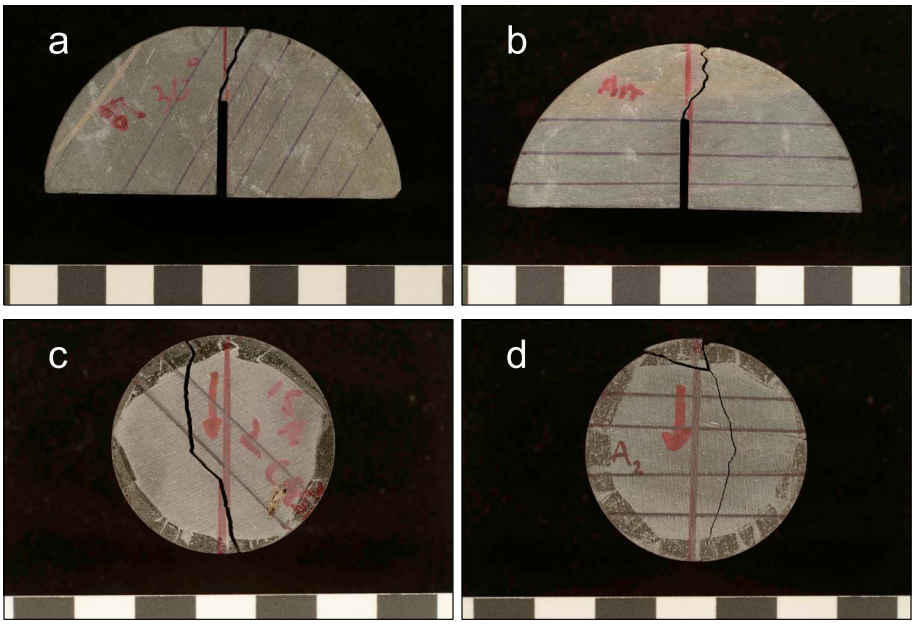

Figure 13. SCB and Brazil disk samples tested oblique to bedding (13a, 13c) and in Arrester orientation (13b, 13d). Solid black lines show the orientation of the bedding plane, and a scale bar lies below each sample where each division is 1 cm. Fractures in these orientations are tortuous and often deflect toward the Short-transverse orientation.

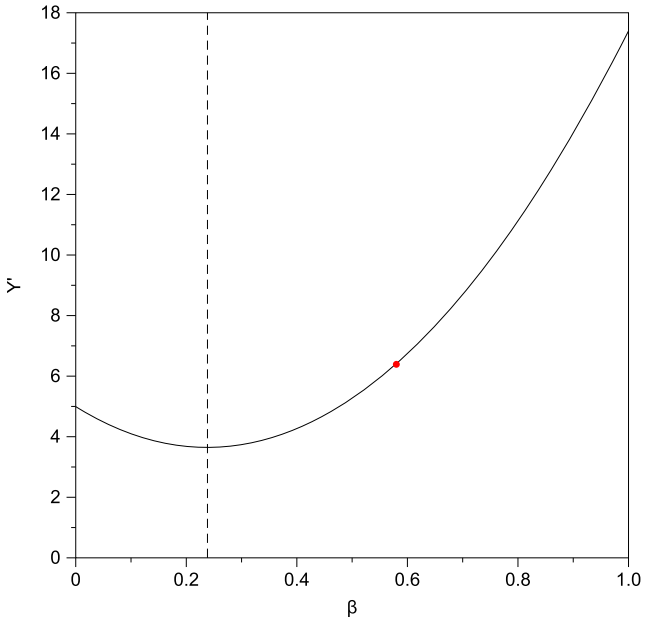

Figure 14. Dimensionless stress intensity factor, Y', as a function of dimensionless fracture length, β, for the semicircular bend (SCB) specimen geometry, calculated from equation (5). The red point shows Y' and β for our chosen notch depth. The vertical dashed line marks the minimum in Y' which separates the region where fracture growth is inherently stable (left of dashed line) from the region where it is inherently unstable (right of dashed line).

dashed line), the fracture propagation is inherently unstable. For this study, we specifically chose sample dimensions so that the values of Y' and β were comfortably within the region of the $Y'(\beta)$ curve where the fracture would always propagate in an unstable (critical) manner (red circle to the right of the vertical dashed line in Figure 14). Under these circumstances, the peak load is recorded at the onset of fracture propagation, and K_{Ic} is therefore also evaluated at this point. Hence, if the fracture deflects after some increment of growth in the correct orientation (e.g., Figure 15a), the fracture toughness evaluation remains valid. Only if the fracture deflection occurs from the initiation point (e.g., Figure 15b) does the calculation become invalid, and the fracture deflection then needs to be accounted for in the evaluation of the fracture toughness.

5.5. Effect of Deflection on Fracture Toughness

When propagating fractures deviate from the intended orientation, they most commonly deflect toward the weaker Short-transverse orientation. An example is shown in Figure 15b. Here the notch is cut at 60° to bedding but the fracture deflects immediately from its initiation point through an angle of approximately 33°, so that it propagates at an angle of 27° to bedding. Under these conditions, the fracture propagates in mixed mode, rather than as a pure mode-I fracture, and we can no longer assume that K_{II} is zero. Furthermore, it is important to recall that, for a sample with a starter notch oriented at angle of ϕ to the Arrester orientation (i.e., 90° − ϕ to bedding), the measured fracture toughness is only valid for that angle if the fracture continues to propagate at angle ϕ at least to the point where the peak load is recorded. If the fracture becomes deflected before this point and propagates at some other angle, ζ, then the apparent fracture toughness evaluated from the peak load K_{Ic} (ζ) needs to be corrected by some geometric factor that takes account of the deflection. The relevant angles for such an analysis are illustrated and defined in Figure 16.

We have therefore developed a method of correcting the measured apparent K_{Ic} for deflections from the initiation path. This allows determination of a deflected-corrected mode-I stress intensity factor, K_{Id}. However, since the deflected fracture propagates in mixed mode, critical crack growth is likely controlled by some combination of K_I and K_{II}, and hence K_{Id} alone cannot be considered a critical value. The two-dimensional symmetry of the SCB specimen, together with direct postmortem measurement of the deflection angle from the sample surface, allows us to use the known stress intensities at the tip of the starter notch and the measured deflection angle to determine the forms of the deflection-corrected mode-I and mode-II stress intensities, K_{Id} and K_{IId}, as set out below.

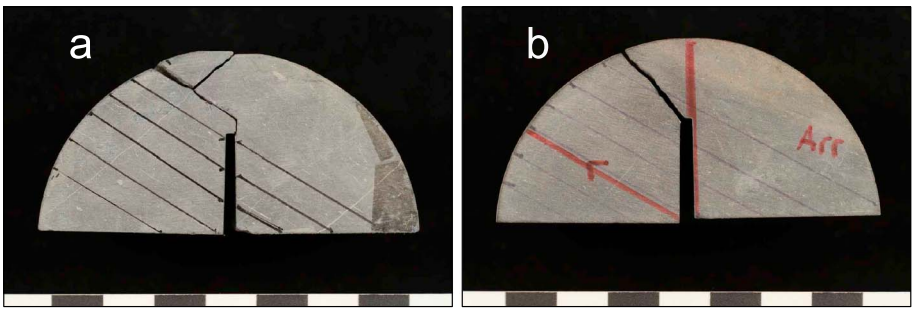

Figure 15. (a) A sample manufactured at 60° to bedding where the fracture has deviated during loading, but not immediately. (b) A fractured sample manufactured at 60° to bedding, in which the fracture immediately deviates to 27° to bedding. Black lines depict the bedding plane, and a scale bar lies below each sample where each division is 1 cm.

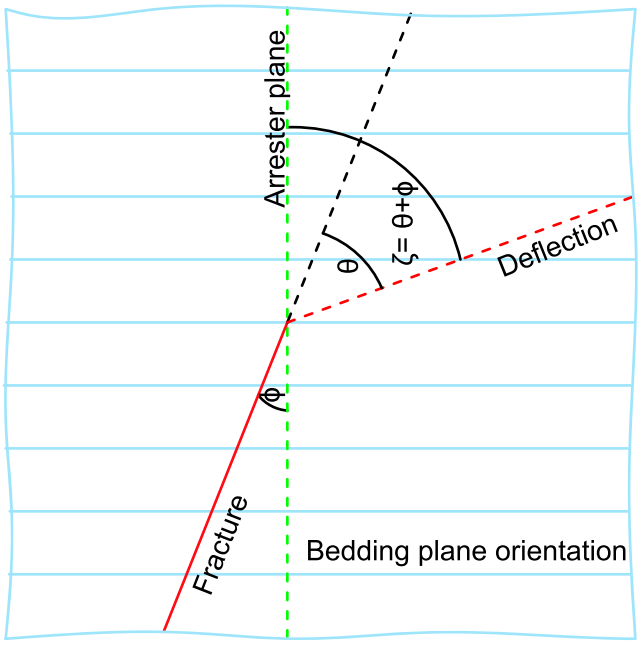

Figure 16. Definitions of the angles used in the analysis here. ϕ is the angle between the initial notch and the Arrester orientation. θ is the angle between the deflected fracture and the initial notch. ζ is the angle between the deflected fracture and the Arrester orientation ($\zeta = \theta + \phi$). Modified after Chandler et al. (2016).

5.6. Stress Intensity at the Tip of a Deflected Fracture

Cotterell and Rice (1980) solved for the mode-I and mode-II stress intensity factors, K_I and K_{II}, at the tip of an infinitesimal deflection of a two-dimensional fracture in an elastically isotropic material from the stress intensities and surface tractions of the initiating deflection. The deflection stress intensity factors, K_{Id} and K_{IId}, are given by

$$K_{Id} = C_{11}K_I + C_{12}K_{II} \tag{7}$$

$$K_{IId} = C_{21}K_I + C_{22}K_{II} \tag{8}$$

where

$$C_{11} = \frac{1}{4}\left[3\cos\left(\frac{\theta}{2}\right) + \cos\left(\frac{3\theta}{2}\right)\right] \tag{9}$$

$$C_{12} = \frac{3}{4}\left[\sin\left(\frac{\theta}{2}\right) + \sin\left(\frac{3\theta}{2}\right)\right] \tag{10}$$

$$C_{21} = \frac{1}{4}\left[\sin\left(\frac{\theta}{2}\right) + \sin\left(\frac{3\theta}{2}\right)\right] \tag{11}$$

$$C_{22} = \frac{1}{4}\left[\cos\left(\frac{\theta}{2}\right) + 3\cos\left(\frac{3\theta}{2}\right)\right] \tag{12}$$

and K_I and K_{II} are the stress intensity factors in the intended fracture orientation and θ is the angle from that orientation at which the deflection initiates. In using equations (7) and (8), which were derived for an elastically isotropic material, we inherently assume that the effect of the fracture toughness anisotropy significantly outweighs any effect of elastic anisotropy. Cotterell and Rice (1980) showed that, for the cases of pure mode-I and mode-II loading of the main fracture, these functions agree with the computations of Bilby et al. (1978) to within 5% and 10%, respectively, for values of θ from 0° to 90°.

Since, for our sample geometry, the peak load is recorded at the onset of fracture growth (as shown in section 5.4), the mode-I stress intensity factor of the main fracture, K_I, can be determined from equation (3) with a' set equal to the modified (actual) notch length, and K_{II} set equal to zero. If θ is set equal to the measured initial deflection angle on the sample surface, then equations (7) and (8) can be used to find the stress intensities at the tip of an infinitesimal deflection in this θ direction. We can therefore use the value of K_{Ic} determined from equation (3), in combination with the measured deflection angle, to determine the deflection-corrected stress intensity values, K_{Id} and K_{IId}, measured at the deflection point, simply from $K_{Id} = C_{11} \times K_{Ic}$, and $K_{IId} = C_{21} \times K_{Ic}$.

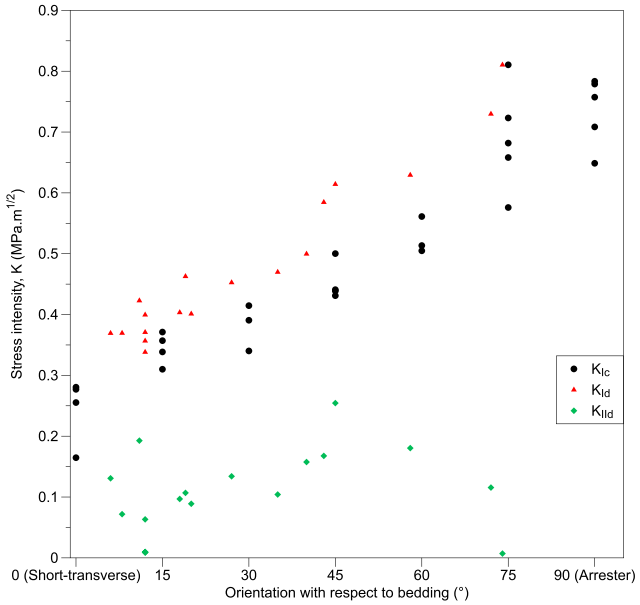

Figure 17. K_{Ic}, K_{Id}, and K_{IId} as a function of orientation from bedding.

Figure 17 shows values of K_{Ic} plotted as a function of orientation to bedding for un-deflected fractures, together with K_{Id} and K_{IId} for deflected fractures, also plotted as functions of orientation to bedding. The magnitude of the correction to K_{Ic} required to obtain the values of K_{Id} for the deflected fractures is seen to be small but systematic, with values of K_{Id} always being slightly higher than K_{Ic} for the same orientation. The calculated values of K_{IId} appear to show no systematic change with orientation across the whole data range and exhibit a mean of 0.11 ± 0.07 MPa $m^{1/2}$. However, since K_{IId} is not negligible with respect to K_{Id}, especially at low angles to bedding, we suggest that a fracture energy-based approach may be more appropriate than a stress intensity-based approach in analyzing the full spectrum of fracture propagation in this material.

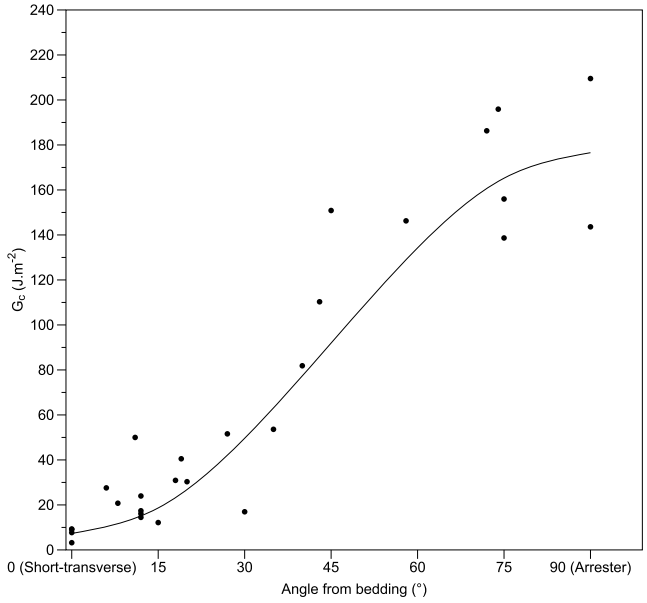

Figure 18. G_c as a function of angle from bedding. The solid curve is derived from equation (17) where $G_{c,Arrester}$ and $G_{c,Short\text{-}transverse}$ are found to be 176.56 J/m^2 and 7.32 J/m^2, respectively.

5.7. Fracture Energy at the Tip of Deflected and Undeflected Fractures

The fracture energy, G, can be determined directly from the stress intensities via

$$G = \frac{1-\nu^2}{E}\left(K_I^2 + K_{II}^2\right) \tag{13}$$

where ν is Poisson's ratio and E is Young's modulus. For the case of a critical undeflected fracture, $K_I = K_{Ic}$ and $K_{II} = 0$. Therefore,

$$G_c = \frac{1-\nu^2}{E}K_{Ic}^2 \tag{14}$$

However, for deflected fractures, $K_I = K_{Id}$ and $K_{II} = K_{IId}$. So we can write

$$G_c = \frac{1-\nu^2}{E}\left({K_{Id}}^2 + {K_{IId}}^2\right) \tag{15}$$

However, for an anisotropic material like shale, the values of Young's modulus and Poisson's ratio will also vary as a function of orientation, as has previously been discussed by Ong et al. (2016) and Meléndez-Martínez and Schmitt (2016). We have therefore measured the static Young's modulus and Poisson's ratio on cylindrical samples of Nash Point shale in both the bedding-normal and bedding-parallel orientations. We have also calculated the dynamic Young's modulus for each orientation using the elastic wave velocity data of Figure 4 and standard relationships (Eissa & Kazi, 1988; King, 1983). Finally, we calculated the static Young's moduli for each orientation by normalizing the end-member dynamic values to the static values measured parallel and normal to bedding, with the assumption that the same relation applies across the whole range of angles. A complete description of the methodology, together with plots of the dynamic and static moduli and a table of all the values used in our calculations of G_c from equations (14) and (15) is presented in the Supporting Information S1. Our measured values of static Poisson's ratio vary by more than a factor of 4 between the bedding-normal and bedding-parallel orientations. However, the expression for Poisson's ratio used in the calculation of G_c is $(1 - \nu^2)$. Substituting our end-member measured values into this expression gives a value of 0.92 ± 0.07, a variation of less than 8%. We have therefore used this mean value in all our calculations of G_c. Again, a full description is provided in the supporting information.

We plot the resulting fracture energies as a function of orientation from bedding in Figure 18. We observe that G_c increases as the angle from bedding increases, but in a nonlinear manner.

Sesetty and Ghassemi (2016) suggested that the fracture toughness of anisotropic materials should vary elliptically with respect to fracture orientation from bedding and that the fracture toughness at any angle (β) between the Short-transverse and Arrester orientations could therefore be approximated by the following relation:

$$K_{Ic,\beta} = K_{Ic,Arrester}\sin^2(\beta) + K_{Ic,Short=transverse}\cos^2(\beta) \tag{16}$$

where β is the angle measured from the Short-transverse orientation. Their suggestion is based on the work of Buczek and Herakovich (1985) who reasoned that the tensile strength of anisotropic rocks varied elliptically between the Short-transverse and Arrester values, and the linear relationship between tensile strength and fracture toughness (equation (6)). However, we find that neither our tensile strength nor our fracture toughness data are well described by such an elliptical approximation. By contrast, we find that an elliptical approximation provides a good fit to the fracture energy data according to

$$G_{c,\beta} = G_{c,Arrester}\sin^2(\beta) + G_{c,Short\text{-}transverse}\cos^2(\beta) \tag{17}$$

We have therefore plotted this function on Figure 18, constrained by our end-member Short-transverse and Arrester values of G_c. While there is clearly some scatter, we find the function fits well, with an R^2 value of 0.90.

We suggest that the reason why fracture energy appears to vary elliptically between the Short-transverse and Arrester orientations, while tensile strength and fracture toughness do not, may well be because fracture energy is able to take account of any fracture propagation with a mixed mode element, while the other parameters are not.

6. Conclusions

We report a study in which we have measured ultrasonic wave velocities, tensile strength, and fracture toughness on samples of Nash Point shale in multiple orientations, including the three principal fracture orientations (Short-transverse, Arrester, and Divider). We used the Brazil disk technique to measure apparent tensile strength and the SCB methodology to measure fracture toughness. It was found that both the apparent tensile strength and the fracture toughness of Nash Point shale were much lower in samples tested in the Short-transverse than in the Arrester orientations. Samples tested in the Divider orientation, produced values that were very similar to samples tested in the Arrester orientation. Both the apparent tensile strength and fracture toughness increased progressively between the Short-transverse and the Arrester orientations.

Fracture deflection was commonly observed in both apparent tensile strength and fracture toughness samples, with fractures deviating from the intended direction toward the weaker Short-transverse orientation. We therefore propose a method of correcting the measured apparent K_{Ic} for fractures that are deflected from the initiation point. This allows the determination of a deflection-corrected mode-I stress intensity factor, K_{Id}. However, since deflected fractures propagate in mixed mode, critical crack growth is likely controlled by some combination of K_I and K_{II}, and hence K_{Id} alone cannot be considered a critical value. We therefore adopted a fracture energy (G_c) based approach to analyze fracture propagation at orientations between the Short-transverse and Arrester orientations and determined the angular variation of G_c.

We observe that G_c increases with increasing angle to bedding, but in a nonlinear manner. Further, we find that the orientation-dependent G_c values are well fit by an elliptical relation with an R^2 value of 0.90. As such we propose that it is possible to calculate a good approximation of G_c values at angles between the Short-transverse and Arrester orientation of an anisotropic material using the approach presenent here and the Short-transverse and Arrester values.

Hydraulic fractures in unconventional oil and gas reservoirs are often modeled as having straight geometries with little or no correction for roughness, tortuosity, or deflection (Li et al., 2017; Wangen, 2017; Zhao et al., 2017). Furthermore, many models also consider reservoirs to be mechanically isotropic (Feng & Gray, 2018; Li et al., 2017; Wangen, 2017; Zhao et al., 2017). Our results demonstrate that neither assumption is likely to be valid either for shale units or reservoirs composed largely of shale. However, the results presented should be useful in the analysis of how fractures may propagate in highly anisotropic rocks, such as shales, especially where the propagation path is oblique to the three principal directions (Short-transverse, Arrester, and Divider). Such analysis may enhance development and management of unconventional oil and gas reservoirs and understanding the integrity of seals in conventional and carbon capture and storage reservoirs.

Acknowledgments
We thank the NERC CDT in Oil and Gas (grant NE/M00578X/1), and Hannon Westwood for supporting N. F. I. through his research, while M. C. acknowledges support from the UK Natural Environment Research Council (grant NE/M001458/1). We also thank Neil Hughes, Steve Boon, Jim Davy, and John Bowles for help with the experimental work, and Nicolas Brantut for his help in analyzing the fracture deflections in the SCB samples. Finally, we thank Stephan Gehne, John Webb, Kathryn Lamb, Emma Davies, John Corr, Jackie Forbes Inskip, Roy Forbes Inskip, Robert Inskip, and Sally Inskip for their help in collecting samples from Nash Point and for their general support. We thank Julia Gale and Douglas Schmitt for thoughtful and detailed comments on an earlier version of this manuscript, which have helped improve the text and clarify the arguments. All data used for this study can be accessed via the data repository Hydroshare: http://www.hydroshare.org/resource/2491340819 3b41caa1896a6e60327946

References

Bhagat, R. (1985). Mode I fracture toughness of coal. *International Journal of Mining Engineering*, *3*(3), 229–236. https://doi.org/10.1007/BF00880769

Bilby, B. A., Cardew, G. E., & Howard, I. C. (1978). Stress intensity factors at the tips of kinked and forked cracks. In D. M. R. Taplin (Ed.), *Advances in research on the strength and fracture of materials* (pp. 197–200). New York: Pergamon. https://doi.org/10.1016/B978-0-08-022142-7.50039-9

Birch, F. (1960). The velocity of compressional waves in rocks to 10 kilobars, Part 1. *Journal of Geophysical Research*, *65*, 1083–1102. https://doi.org/10.1029/JZ065i004p01083

Boyer, C., Lewis, R., Miller, C. K., & Clark, B. (2011). Shale gas: A global resource. Oilfield Review.

Buczek, M. B., & Herakovich, C. T. (1985). A normal stress criterion for crack extension direction in orthotropic composite materials. *Journal of Composite Materials*, *19*(6), 544–553. https://doi.org/10.1177/002199838501900606

Chalmers, G. R. L., & Bustin, R. M. (2017). A multidisciplinary approach in determining the maceral (kerogen type) and mineralogical composition of Upper Cretaceous Eagle Ford Formation: Impact on pore development and pore size distribution. *International Journal of Coal Geology*, *171*, 93–110. https://doi.org/10.1016/j.coal.2017.01.004

Chandler, M. R. (2014). A fracture mechanics study of an anisotropic shale. Univeristy College London.

Chandler, M. R., Meredith, P. G., Brantut, N., & Crawford, B. R. (2016). Fracture toughness anisotropy in shale. *Journal of Geophysical Research: Solid Earth*, *121*, 1706–1729. https://doi.org/10.1002/2015JB012756

Chen, C., Pan, E. & Amadei, B. (1998). Determination of deformability and tensile strength of anisotropic rock using Brazilian tests. *International Journal of Rock Mechanics and Mining Sciences*, *35*(1), 43–61. https://doi.org/10.1016/S0148-9062(97)00329-X

Chong, K. P., Kuruppu, M. D., & Kuszmaul, J. S. (1987). Fracture toughness determination of layered materials. *Engineering Fracture Mechanics*, *28*(1), 43–54. https://doi.org/10.1016/0013-7944(87)90118-4

Claesson, J., & Bohloli, B. (2002). Brazilian test: Stress field and tensile strength of anisotropic rocks using an analytical solution. *International Journal of Rock Mechanics and Mining Sciences*, *39*(8), 991–1004. https://doi.org/10.1016/S1365-1609(02)00099-0

Cornford, C. (1986). The Bristol Channel graben: Organic geochemical limits on subsidence and speculation on the origin of inversion. *Geoscience in South-West England*, *6*(3), 360–367.

Cotterell, B., & Rice, J. R. (1980). Slightly curved or kinked cracks. *International Journal of Fracture*, *16*(2), 155–169. https://doi.org/10.1007/BF00012619

Dewhurst, D. N., & Siggins, A. F. (2006). Impact of fabric, microcracks and stress field on shale anisotropy. *Geophysical Journal International*, *165*, 135–148.

Eissa, E. A., & Kazi, A. (1988). Relation between static and dynamic Young's moduli of rocks. *International Journal of Rock Mechanics and Mining Sciences And*, *25*(6), 479–482. https://doi.org/10.1016/0148-9062(88)90987-4

Elston, H. W. (2014). Mineralogical and geochemical assessment of the Eagle Ford shale. Ohio State University.

Feng, Y., & Gray, K. E. (2018). Modeling of curving hydraulic fracture propagation from a wellbore in a poroelastic medium. *Journal of Natural Gas Science and Engineering*, *53*, 83–93. https://doi.org/10.1016/j.jngse.2018.02.020

Gunsallus, K. L., & Kulhawy, F. H. (1984). A comparative evaluation of rock strength measures. *International Journal of Rock Mechanics and Mining Sciences and Geomechanics*, *21*(5), 233–248. https://doi.org/10.1016/0148-9062(84)92680-9

Heap, M. J., Vinciguerra, S., & Meredith, P. G. (2009). The evolution of elastic moduli with increasing crack damage during cyclic stressing of a basalt from Mt. Etna volcano. *Tectonophysics*, *471*(1–2), 153–160. https://doi.org/10.1016/j.tecto.2008.10.004

International Society for Rock Mechanics (1978). Suggested methods for determining tensile strength of rock materials. *International Journal of Rock Mechanics and Mining Sciences and Geomechanics*, *15*(3), 99–103. https://doi.org/10.1016/0148-9062(78)90003-7

International Society for Rock Mechanics (1988). Suggested methods for determining the fracture toughness of rock. *International Journal of Rock Mechanics and Mining Science and Geomechanics Abstracts*, *33*(8), 803–847. https://doi.org/10.1016/S0148-9062(96)00015-0

Islam, M. A., & Skalle, P. (2013). An experimental investigation of shale mechanical properties through drained and undrained test mechanisms. *Rock Mechanics and Rock Engineering*, *46*(6), 1391–1413. https://doi.org/10.1007/s00603-013-0377-8

Johnston, J. E., & Christensen, N. I. (1995). Seismic anisotropy of shales. *Journal of Geophysical Research*, *100*(B4), 5991–6003.

Kabir, P., Ulm, F.-J., & Akono, A.-T. (2017). Rate-independent fracture toughness of gray and black kerogen-rich shales. *Acta Geotechnica*. https://doi.org/10.1007/s11440-017-0562-0

King, M. S. (1983). Static and dynamic elastic properties of rocks from the Canadian shield. *International Journal of Rock Mechanics and Mining Science and Geomechanics Abstracts*, *20*(5), 237–241. https://doi.org/10.1016/0148-9062(83)90004-9

Knorr, A. F. (2016). The effect of rock properties on fracture conductivity in the Eagle Ford. SPE Asia Pacific Hydraulic Fracturing Conference. Texas A&M University. https://doi.org/10.2118/181867-MS

Kuruppu, M. D., Obara, Y., Ayatollahi, M. R., Chong, K. P., & Funatsu, T. (2014). ISRM-suggested method for determining the Mode I static fracture toughness using semi-circular bend specimen. In R. Ulusay (Ed.), *The ISRM suggested methods for rock characterization, testing and monitoring 2007–2014* (pp. 107–114). Wien: Springer.

Lee, H. P., Olson, J. E., Holder, J., Gale, J. F. W., & Myers, R. D. (2015). The interaction of propagating opening mode fractures with preexisting discontinuities in shale. *Journal of Geophysical Research: Solid Earth*, *120*, 169–181. https://doi.org/10.1002/2014JB011358

Levine, J. S., Fukai, I., Soeder, D. J., Bromhal, G., Dilmore, R. M., Guthrie, G. D., et al. (2016). U.S. DOE NETL methodology for estimating the prospective CO_2 storage resource of shales at the national and regional scale. *International Journal of Greenhouse Gas Control*, *51*, 81–94. https://doi.org/10.1016/j.ijggc.2016.04.028

Li, W., Rezakhani, R., Jin, C., Zhou, X., & Cusatis, G. (2017). A multiscale framework for the simulation of the anisotropic mechanical behavior of shale. *International Journal for Numerical and Analytical Methods in Geomechanics*, *41*(14), 1494–1522. https://doi.org/10.1002/nag.2684

Meléndez-Martínez, J., & Schmitt, D. R. (2016). A comparative study of the anisotropic dynamic and static elastic moduli of unconventional reservoir shales: Implication for geomechanical investigations. *Geophysics*, *81*(3), D245–D261. https://doi.org/10.1190/geo2015-0427.1

Milliken, K. L., Ergene, S. M., & Ozkan, A. (2016). Quartz types, authigenic and detrital, in the upper cretaceous eagle ford formation, South Texas, USA. *Sedimentary Geology*, *339*, 273–288. https://doi.org/10.1016/j.sedgeo.2016.03.012

Mokhtari, M. (2015). Characterization of anisotropy in organic-rich shales: Shear and tensile failure, wave velocity, matrix and fracture permeability. Colorado School of Mines.

Mullen, J., Lowry, J. C., & Nwabuoku, K. C. (2010). Lessons learned developing the Eagle Ford shale. In *SPE Tight Gas Completions Conference* (pp. 2–3). https://doi.org/10.2118/138446-MS

Na, S. H., Sun, W. C., Ingraham, M. D., & Yoon, H. (2017). Effects of spatial heterogeneity and material anisotropy on the fracture pattern and macroscopic effective toughness of Mancos shale in Brazilian tests. *Journal of Geophysical Research: Solid Earth*, *122*, 6202–6230. https://doi.org/10.1002/2016JB013374

Ong, O. N., Schmitt, D. R., Kofman, R. S., & Haug, K. (2016). Static and dynamic pressure sensitivity anisotropy of a calcareous shale. *Geophysical Prospecting*, *64*(4), 875–897. https://doi.org/10.1111/1365-2478.12403

Paterson, M. S., & Wong, T. (2005). *experimental rock deformation—The brittle field*. Berlin: Springer.

Rybacki, E., Reinicke, A., Meier, T., Makasi, M., & Dresen, G. (2015). What controls the mechanical properties of shale rocks?—Part I: Strength and Young's modulus. *Journal of Petroleum Science and Engineering*, *135*, 702–722. https://doi.org/10.1016/j.petrol.2015.10.028

Schmidt, R. A. (1977). Fracture mechanics of oil shale—Unconfined fracture toughness, stress corrosion cracking, and tension test results. In *The 18th U.S. Symposium on Rock Mechanics (USRMS)*. American Rock Mechanics Association.

Sesetty, V., & Ghassemi, A. (2016). Numerical modeling of hydraulic fracture propagation from horizontal wells in anisotropic shale. 50th US Rock Mechanics/Geomechanics Symposium.

Tavallali, A., & Vervoort, A. (2013). Behaviour of layered sandstone under Brazilian test conditions: Layer orientation and shape effects. *Journal of Rock Mechanics and Geotechnical Engineering*, *5*(5), 366–377. https://doi.org/10.1016/j.jrmge.2013.01.004

Vinciguerra, S., Trovato, C., Meredith, P. G., & Benson, P. M. (2005). Relating seismic velocities, thermal cracking and permeability in Mt. Etna and Iceland basalts. *International Journal of Rock Mechanics and Mining Sciences*, *42*(7-8), 900–910. https://doi.org/10.1016/j.ijrmms.2005.05.022

Wangen, M. (2017). A 2D volume conservative numerical model of hydraulic fracturing. *Computers and Structures*, *182*, 448–458. https://doi.org/10.1016/j.compstruc.2017.01.003

Warpinski, N., & Smith, M. B. (1990). Rock mechanics and fracture geometry. In J. L. Gidley, S. A. Holditch, D. E. Nierode, & R. W. Veatch, Jr. (Eds.), *Recent advances in Hydraulic Fracturing* (pp. 57–80). Richardson, TX: Society of Petroleum Engineers.

Young, C., Patti, N. C., & Trent, B. C. (1982). *Stratigraphic variations in oil shale fracture properties*. Larime, Wyoming: USA Department of Energy.

Zhang, Z. X. (2002). An empirical relation between mode I fracture toughness and the tensile strength of rock. *International Journal of Rock Mechanics and Mining Sciences*, *39*(3), 401–406. https://doi.org/10.1016/S1365-1609(02)00032-1

Zhao, J., Chen, X., Li, Y., Fu, B., & Xu, W. (2017). Numerical simulation of multi-stage fracturing and optimization of perforation in a horizontal well. *Petroleum Exploration and Development*, *44*(1), 119–126. https://doi.org/10.1016/S1876-3804(17)30015-0